forests

MDPI

Article

Spatiotemporal Variation in Extreme Climate in the Yellow River Basin and its Impacts on Vegetation Coverage

Zichuang Li [1], Huazhu Xue [1], Guotao Dong [2,3,*], Xiaomin Liu [1] and Yaokang Lian [2]

[1] School of Surveying and Land Information Engineering, Henan Polytechnic University, Jiaozuo 454003, China; xhz@hpu.edu.cn (H.X.)
[2] Heihe Water Resources and Ecological Protection Research Center, Lanzhou 730030, China
[3] Yellow River Conservancy Commission, Yellow River Institute of Hydraulic Research, Zhengzhou 450003, China
* Correspondence: dongguotao001@163.com; Tel.: +86-13523063035

Abstract: Global warming and extreme climate events (ECEs) have grown more frequent, and it is essential to investigate the influences of ECEs on vegetation in the Yellow River Basin (YRB) and other environmentally fragile areas. This study was based on data from 86 meteorological stations in the YRB for the period 2000–2020. Twenty-five extreme climate indices (*ECI*s) were chosen, encompassing four dimensions: extreme value, intensity, duration, and frequency. The trend analysis approach was used to examine the spatiotemporal characteristics of extreme climate conditions. Additionally, geographical detectors and Pearson correlation analysis methods were employed to quantitatively assess the influence of ECEs on the Normalized Difference Vegetation Index (NDVI). The Multiscale Geographically Weighted Regression (MGWR) method was adopted to analyze the regression of twenty-five *ECI*s. The findings revealed the following: (1) Over the last 21 years, there has been a distinct rise in both the extreme precipitation indices (*EPI*s) and the extreme temperature indices (*ETI*s). (2) The spatial distribution of the NDVI throughout the year displayed the characteristic of being high in the south and low in the north. The annual NDVI demonstrated a noteworthy increase at a rate of 0.055/decade, with the enhancement encompassing an extensive area of 87.33%. (3) The investigation revealed that *EPI*s, including PRCPTOT, R10mm, CWD, R95p, and CDD, had explanatory values surpassing 0.4. This implied that the intensity, frequency, and duration of extreme precipitation played pivotal roles in steering vegetation alterations in the YRB. (4) The correlation between the *EPI*s and vegetation was greater than the *ETI*s. Grassland meadows exhibited greater sensitivity to precipitation than woody plants. The *EPI*s (excluding CDD and SDII) and the *ETI*s (TXn) displayed a substantial positive correlation with the NDVI in regions hosting grasslands, broadleaf forests, and shrubs. Desert vegetation and cultivated plants were less affected by ECEs. This study underscores the importance of the interplay between extreme climate and vegetation in the YRB. Additionally, it provides a scientific basis for formulating environmental safeguarding strategies.

Keywords: extreme climate events; NDVI; Yellow River Basin; spatiotemporal change; geographical detector

Citation: Li, Z.; Xue, H.; Dong, G.; Liu, X.; Lian, Y. Spatiotemporal Variation in Extreme Climate in the Yellow River Basin and its Impacts on Vegetation Coverage. *Forests* **2024**, *15*, 307. https://doi.org/10.3390/f15020307

Academic Editor: Xiuchen Wu

Received: 15 December 2023
Revised: 29 January 2024
Accepted: 4 February 2024
Published: 6 February 2024

1. Introduction

Extreme climate events (ECEs) like rainstorms, floods, droughts, and global warming have occurred in recent years, and the area of vegetation affected has increased [1,2]. Global warming has caused an upward trend in the frequency and intensity of ECEs [3]. The term "extreme climate events" typically refers to specific climate factors that surpass both the upper and lower bounds of statistical or observational average climate factors [4]. Earlier studies have indicated that extreme heat events have occurred frequently over the past century [5]. For instance, researchers have studied ECEs spatiotemporal patterns at different scales [6]: the national scale, as represented by China [7]; the Americas [8]; and the local scale, with three major river basins in China serving as study systems [9]. More researchers

have started to simulate extreme climate using the CMIP6 and CMIP5 frameworks [10,11]. Additionally, there is still a possibility of extreme climate conditions breaking records due to carbon emission levels [12]. Regarding extreme climate research in China, some scholars have found that extreme warmth will increase in Northern and Western China, while cold events will decrease. A significant increase in maximum continuous five-day precipitation events and precipitation intensity were expected in China, while continuous drought events in the northern and western parts were expected to decline significantly [13]. The relationship between terrestrial ecosystems and climate variation continues to receive international attention, and monitoring the dynamics of climate extremes and their impacts on vegetation is a hot topic in regional vegetation research.

Vegetation performs a vital role in ecological services such as climate regulation and biodiversity [14,15]. The Normalized Difference Vegetation Index (NDVI) is a powerful metric for characterizing changes in surface vegetation coverage at large scales [16]. It can accurately characterize the vegetation change in a region and is usually used as a measure of ecological impacts on vegetation. In recent years, domestic and international scholars have separately studied the link between NDVI variations and climate changes at the global, national, and regional scales [17–20]. These studies have demonstrated that a good coupling of hydrothermal conditions is a necessary condition for vegetation growth. In terms of impacts on vegetation dynamics, extreme climate change (ECC) had a much larger effect than average climate change (ACC) [21]. However, most of the aforementioned studies have concentrated on the response of vegetation to average climatic conditions, while studies on the impact of ECC on vegetation are lacking. Therefore, investigating the response of vegetation to ECEs is a hot topic of modern research.

The Yellow River Basin (YRB) spans the eastern, central, and western regions and flows through nine provinces and regions with a wide range of influences. The river is an essential ecological buffer zone in China, and the mother river is key to the water requirements of the local population [22]. Historically, this area has been prone to natural disasters and is characterized by an uneven distribution and scarcity of water resources, making it a typical arid-semiarid region [23]. General Secretary Xi has repeatedly emphasized that ecological protection and high-quality development in the YRB are major national land use strategies [24]. We urgently are required to protect the ecological environment of the YRB, address the water and sediment relationship, and alleviate the supply-demand tension over its water resources [25]. The Yellow River Conservation Project has been launched and has made significant accomplishments in the management of this region [26]. In addition to focusing on key ecological areas in the YRB, we will diligently carry out projects such as comprehensive land improvement and the construction of protective forest systems, such as the Three North project, so as to reduce soil erosion. However, there are still pressing issues that need to be addressed. Against the backdrop of global climate warming, the YRB is experiencing a trend of rising temperatures, with a growing number of extreme heat events [9]. The trend of annual extreme heavy rainfall exhibits distinct regional differences, with a decrease in the duration of *EPI*s [27]. The YRB is a region sensitive to climate variations and is ecologically vulnerable [28]. Extreme climate events pose severe challenges to its water resources, ecological environment, and food security. Therefore, studying and evaluating the evolving spatiotemporal characteristics of ECEs in the region and their impact on vegetation has important practical value and is conducive to preventing and resolving ecological security risks. Such research fulfills a practical need for informing the building of a beautiful China.

In large-scale studies, differences in surface ecological environments can lead to different vegetation responses to climate change. The analysis of spatiotemporal variations in regional vegetation and climate characteristics from a subbasin perspective is particularly important. This study was based on data from 86 meteorological stations in the YRB for the period 2000–2020. Using 25 *ECI*s suggested by the World Meteorological Organization, we comprehensively analyzed the spatiotemporal characteristics of ECEs using four categories: extremes, intensity, duration, and frequency. By combining the contemporaneous MODIS

NDVI data, we utilized a geographical detector for the driving force analysis of the impact of ECEs on vegetation cover. Then, we analyzed whether the spatial heterogeneity of the dominant drivers of ECEs had an effect on the vegetation cover of YRB using MGWR. We also focused on the response of different vegetation types to ECEs. The aim is to provide scientific evidence for understanding regional ecosystem dynamics, studying ecosystem vulnerability, and predicting future climate change.

2. Materials and Methods

2.1. Study Area

The Yellow River Basin (YRB) is located between 32° N–42° N and 96° E–119° E. It begins from the Bayan Har Mountains in the west and flows to the Bohai Sea, starting from the Yin Mountain in the north and stretching to the Qinling Mountains (Figure 1a). The terrain of the basin gradually declines from west to east. To the west are the headwaters of the river basin, which consists of a series of high mountains averaging more than 4000 m above sea level. To the north is the Inner Mongolian Plateau, with elevations ranging from 1300 to 2200 m. The northern side is bordered by the Yin Mountains, while the western side is the Helan Mountains. In the middle, there are some fragmented basins and the Ordos Plateau. The central region is the Loess Plateau, with elevations ranging from 1000 to 2000 m. The dominant landform is loess-covered tablelands and hills, which suffer from significant soil loss. The downstream area is the Huang-Huai-Hai Plain, characterized by lower elevation.

Typical arid, semi-arid, and alpine regions exist in the study area. Regional temperature variations are significant, and the spatial distribution pattern is low in the northwest and high in the southeast. These landforms and climatic features determine regional variations in vegetation types and coverage (Figure 1b). The river source region is controlled by low temperatures and dominated by alpine vegetation, including alpine shrubs, alpine meadows, alpine grasslands, marshes, and aquatic vegetation. The Loess Plateau is characterized by forests and grasslands as the dominant vegetation types, and it gradually transitions from grasslands in the west to forest-steppe.

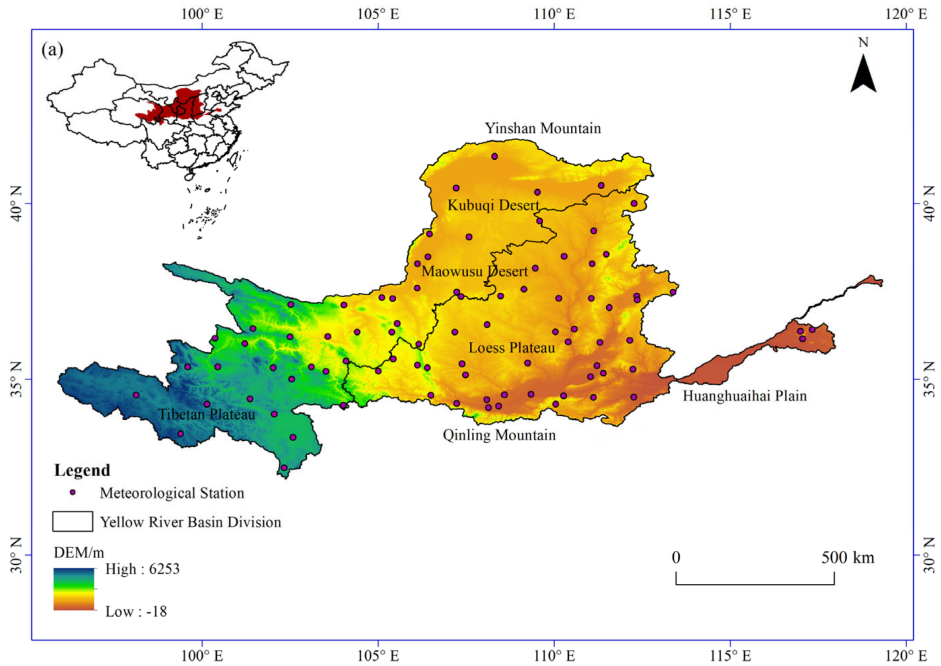

Figure 1. *Cont.*

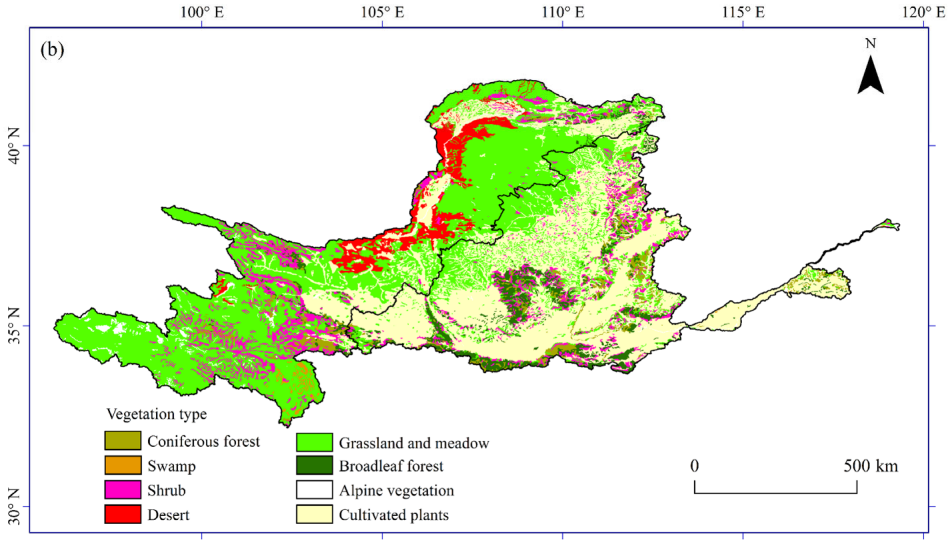

Figure 1. (**a**) Meteorological station, DEM, and YRB division; and (**b**) vegetation types in the Yellow River Basin.

2.2. Data Sources and Processing

The NDVI data were derived from the MOD13Q1 dataset (https://earthengine.google.com/). To better represent the vegetation coverage on the land surface, the maximum value composite (MVC) method [29,30] was adopted to generate annual NDVI data for the years 2000–2020, which were employed in the analysis of the spatiotemporal variation in vegetation cover and its response to ECEs in the YRB.

The climatological data were downloaded from the National Meteorological Science Data Center (https://data.cma.cn/). A total of 86 meteorological stations in the YRB with complete and consistent time series data from 2000 to 2020 were selected. Daily minimum and maximum temperature and daily precipitation data were used to calculate 25 *ECI*s using RClimDex1.1 software (Toronto, ON, Canada). These indices include 11 *EPI*s and 14 *ETI*s. Spatial interpolation was performed using the kriging method, and the selected extreme climate indices were classified into four categories: extremes, intensity, duration, and frequency. The definitions of 25 *ECI*s are provided in Table 1.

Table 1. Classification and description of 25 extreme climate indices.

Classification	Extreme Climate Indices	Description	Unit
Precipitation intensity index	Rx1day	Maximum 1-day precipitation	mm
	Rx5day	Maximum 5-day precipitation	mm
	PRCPTOT	Annual total precipitation on wet days	mm
	SDII	Simple daily precipitation intensity index	mm/d
	R95p	Annual contribution from very wet days (daily precipitation is greater than the 95th percentile of precipitation)	mm
	R99p	Annual contribution from extremely wet days (daily precipitation is greater than the 99th percentile of precipitation)	mm
Precipitation persistence index	CDD	Maximum length of dry spell, maximum number of consecutive days with daily precipitation less than 1 mm	Days
	CWD	Maximum length of wet spell; maximum number of consecutive days with daily precipitation greater than 1 mm	Days
Precipitation frequency index	R10mm	Annual count of days when daily precipitation is greater or equal to 10 mm	Days
	R20mm	Annual count of days when daily precipitation is greater or equal to 20 mm	Days
	R25mm	Annual count of days when daily precipitation is greater or equal to 25 mm	Days

Table 1. *Cont.*

Classification	Extreme Climate Indices	Description	Unit
Cold extreme temperature	TX10p	Percentage of days when the daily maximum temperature is less than that of the 10th percentile	%
	TN10p	Percentage of days when the daily minimum temperature is less than that of the 10th percentile	%
	TNn	The minimum value of the daily minimum temperature	°C
	TXn	Minimum value of daily maximum temperature	°C
	FD	Number of frost days	Days
Warm extreme temperature	TX90p	Percentage of days when the daily maximum temperature is greater than the 90th percentile	%
	TN90p	Percentage of days when the daily minimum temperature is greater than the 90th percentile	%
	TNx	The maximum value of the daily minimum temperature	°C
	TXx	Maximum value of daily maximum temperature	°C
	SU	Number of summer days	Days
Temperature intensity index	DTR	Daily temperature range	°C
Temperature persistence index	GSL	Growing season length	Days
	WSDI	Warm spell duration index	Days
	CSDI	Cold spell duration index	Days

2.3. Analysis Procedure

First, the daily minimum and maximum temperature and daily precipitation data for the period 2000–2020 were extracted from 86 meteorological stations within the YRB. RClimDex1.1 software was used to calculate 25 *ECI*s. Then, the spatiotemporal trends of the *ECI*s and the vegetation NDVI in the Yellow River subbasins were characterized with the Theil-Sen method. The Mann-Kendall method was also utilized to check the significance of the trends. The factor explanatory power of the 25 *ECI*s on the NDVI was investigated using geographical detectors. Additionally, the link between the vegetation NDVI and *ECI*s was examined using the Pearson correlation coefficient method.

2.4. Methods

2.4.1. Theil-Sen Trend Analysis Method

The Theil-Sen slope method does not assume any specific distribution of the data and is widely used to calculate regional trends due to its robustness properties [31]. In this study, the image-by-image approach was adopted to use the Theil-Sen slope method that calculates the spatial trend value of *ECI*s and the NDVI. $|Z| > 1.96$ indicates a significant change in the *ECI*s based on a 95% significance level. The formula is as follows:

$$S = median\left(\frac{x_j - x_i}{t_j - t_i}\right), 2000 \le i < j \le 2020 \quad (1)$$

The formula includes the median function, S representing the *ECI*s or the NDVI trend, x_i and x_j representing the sequence data for different years, and t_i and t_j representing the study time period. $S > 0$ and $S < 0$ indicate upward and downward trends, respectively.

In addition, the Mann-Kendall (M-K) trend test has the advantage of nonparametric statistics and has been used extensively in combination with Theil-Sen in hydrological, meteorological, and other time series trend analysis [32–34]. It is not limited by data distribution or a few outliers. This method is designed to test the significance of variability in *ECI*s and the NDVI [21].

2.4.2. Geographical Detector Model

The geographical detector model (GDM) is a statistical methodology for detecting spatial differences and revealing underlying driving forces [35,36]. In this research, factor detectors were employed to quantitatively analyze the driving force of the 25 *ECI*s in the YRB for the NDVI variation. The specific calculation is described below:

$$q = 1 - \sum_{h=1}^{L} \frac{N_h \sigma_h^2}{N\sigma^2} \quad (2)$$

where q represents the driving force of the *ECI*s on the NDVI trend.

The q value ranges from 0 to 1, with higher values indicating greater explanatory power, and h (1, 2, …, L) represents variable classification or partitioning. N_h and N represent the number of cells in stratum h and the whole region, and ${\sigma_h}^2$ and σ^2 represent the variance of Y values in stratum h and the region, respectively.

The interaction detector can identify the interaction effects between different extreme climate indices. The evaluation is performed by calculating and comparing the q values of the individual and joint explanatory power of the two factors X1 and X2 for Y: q(X1), q(X2), and q(X1∩X2). Factor interaction categorization can be found in the original study [35].

2.4.3. Pearson Correlation Coefficient

The Pearson correlation coefficient method was adopted to explore the correlation between *ECI*s and the NDVI [37]. The specific calculation is described below:

$$R = \frac{\sum_{i=1}^{n} \left(ECIs_i - \overline{ECIs}\right)\left(NDVI_i - \overline{NDVI}\right)}{\sqrt{\sum_{i=1}^{n} \left(ECIs_i - \overline{ECIs}\right)^2 \sum_{i=1}^{n} \left(NDVI_i - \overline{NDVI}\right)^2}} \quad (3)$$

R represents the correlation coefficient between the *ECIs* and the NDVI. It ranges from −1 to 1. *NDVIi* denotes the NDVI value for year i, ($\overline{NDVI}$)represents the average NDVI value over multiple years, $ECIs_i$ represents the *ETI*s or *EPI*s value for year i, and ($\overline{ECIs}$)represents the average *ETI*s or *EPI*s over multiple years. The larger the R value, the stronger the correlation between the variables. Significance testing was performed using the t-statistic.

2.4.4. Multiscale Geographically Weighted Regression

The ordinary least squares (OLS) method assumes that regression parameters remain constant in space and is a traditional global regression approach. It overlooks the spatial heterogeneity existing between the NDVI and various explanatory variables [38,39].

Geographically weighted regression (GWR) can establish local regression models for each location, offering benefits in capturing spatially heterogeneous between explanatory and responsive variables and fully accounting for spatial variation to yield improved regression outcomes [40,41].

In comparison to GWR, multiscale geographically weighted regression (MGWR) is not confined to fixed bandwidths and provides more diverse spatial scales for various variables [42]. It selects optimal spatial scales for different processes, achieving optimal parameter estimates at varying stages of spatial heterogeneity. Furthermore, it can reduce multicollinearity and provide more accurate parameter estimates [43]. The MGWR model can be formulated as follows:

$$y_i = \sum_{j=0}^{m} \beta_{bwj}(\mu_i, v_i) x_{ij} + \varepsilon_i \quad (4)$$

where bwj in β_{bwj} denotes the bandwidth to be used to calibrate the j-th conditional relationship.

Prior to performing MGWR, the variance inflation factor (VIF) was calculated for diagnosing multicollinearity, examining whether there is redundancy in the explanatory power of the selected driving factors with respect to the NDVI, and eliminating driving factors that fail the test. Additionally, combining the factor detector results of the geographical detector, driving factors were further determined. The diagnostic results of multiple covariates for the different drivers are presented in Table 2.

Table 2. MGWR multicollinearity diagnostic results.

2000	VIF Value	2005	VIF Value	2010	VIF Value	2015	VIF Value	2020	VIF Value
PRCPTOT	4.494	PRCPTOT	8.911	PRCPTOT	9.156	PRCPTOT	8.857	PRCPTOT	7.706
R10mm	5.439	R10mm	5.216	R10mm	6.348	R10mm	6.741	R99p	3.566
FD	3.883	R95p	5.074	R95p	8.291	R95p	2.872	R95p	9.112
DTR	4.009	Rx5day	3.880					Rx5day	2.4

3. Results

3.1. Variation Characteristics of Extreme Climate Indices in the YRB

3.1.1. Temporal Dynamics of the Extreme Precipitation Indices

The temporal trends of the *EPI*s in the YRB from 2000 to 2020 indicated an increasing trend for precipitation intensity (Figure 2). Rx1day and Rx5day exhibited increasing rates of 1.910 and 5.535 mm/decade, respectively, suggesting an increasing intensity of *EPI*s on both daily and continuous scales (Figure 2a). PRCPTOT had a growth rate of 45.846 mm/decade, while SDII had a growth rate of 0.483 (mm/d)/decade (Figure 2b,c). R95p and R99p showed upward trends at rates of increase of 20.742 mm/a and 6.999 mm/a, respectively, demonstrating a steady increase in precipitation intensity (Figure 2d). CDD decreased at a rate of 0.200 d/decade, while CWD increased at a rate of 0.123 d/decade (Figure 2e). The precipitation frequency indices R10mm, R20mm, and R25mm exhibited weak increasing rates of 1.758 d/decade, 0.862 d/decade, and 0.548 d/decade, respectively (Figure 2f). As a result, extreme precipitation intensity, duration, and frequency had an upward trend from 2000 to 2020. Furthermore, the maximum values of *EPI*s such as PRCPTOT, R10mm, and R20mm occurred in 2003, while the minimum values of Rx1day, Rx5day, SDII, R95p, R99p, R20mm, and R25mm were observed in 2015.

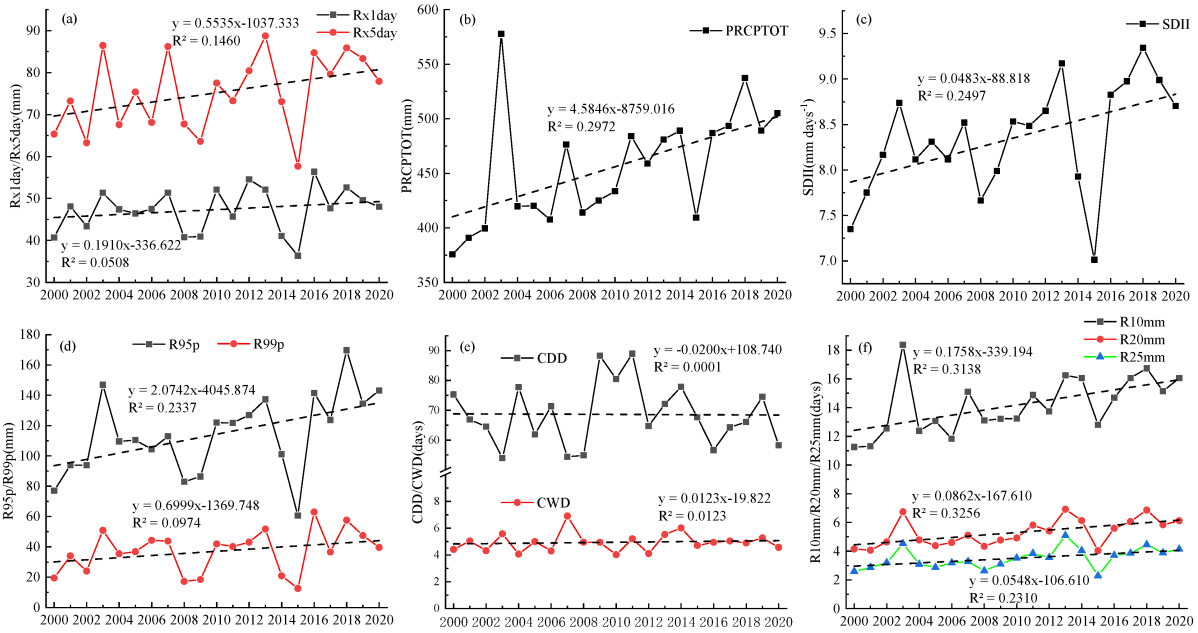

Figure 2. Temporal variations in the 11 extreme precipitation indices (**a**–**f**). The black dotted line represents the trend of the variable during 2000–2020.

3.1.2. Spatial Evolution in Extreme Precipitation Indices

From Figure 3, it was found that 27.43% of the area of Rx1day had an increasing trend, and 72.57% had a decreasing trend. A total of 37.13% of the area of Rx5day increased, and 62.87% of the area decreased. PRCPTOT exhibited an upward trend of 60.19% and a downward trend of 39.81%. The areas where Rx1day and PRCPTOT exhibited a remarkable increasing trend were mainly located in the downstream Huang-Huai-Hai Plain, while the regions with an upward trend for Rx5day were primarily found in the western upstream and northeastern regions but not significantly (Figure 4a,c). A total of 56.31% of the area of SDII exhibited an upward trend, but this trend was significant. R95p and R99p showed decreasing areas of 64.51% and 64.56%, respectively, located in the upstream eastern and midstream, while the increasing areas accounted for 35.49% and 35.44%, mainly located in the downstream eastern (Figure 4e,f). This indicated that extreme precipitation intensity has increased in the upstream western and downstream over the past 21 years, while it has decreased in the upstream eastern and midstream.

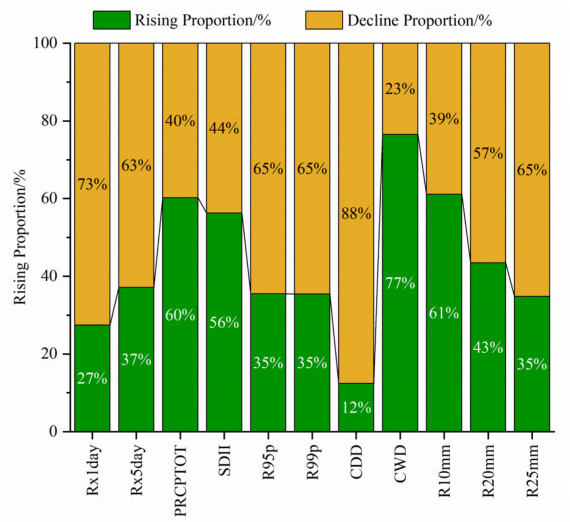

Figure 3. Area changes in the 11 extreme precipitation indices during 2000–2020.

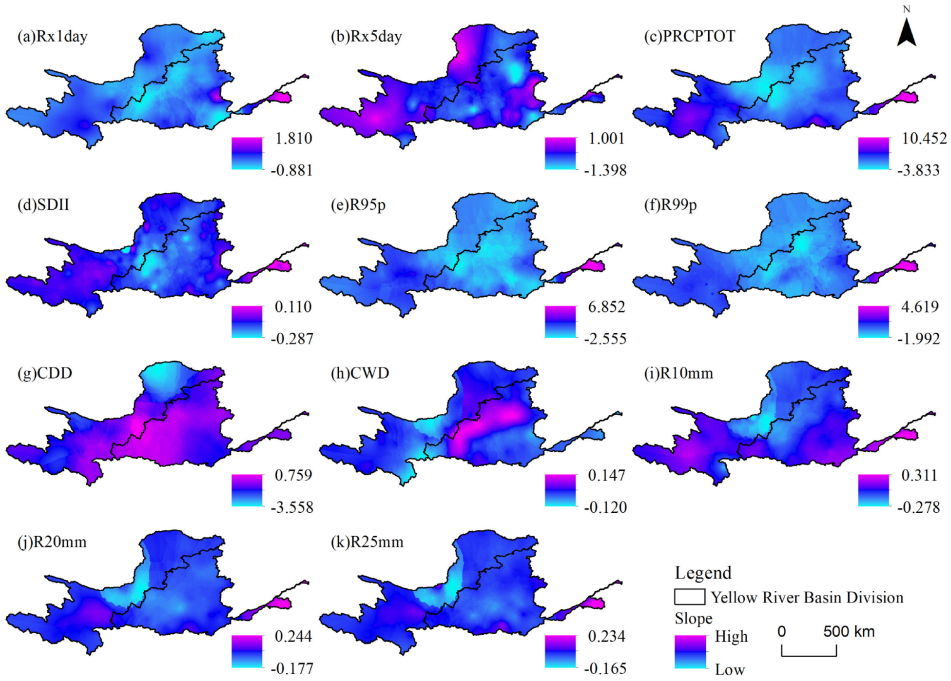

Figure 4. Spatial distribution of the 11 extreme precipitation indices from 2000 to 2020 in YRB.

A total of 87.61% of the CDD districts decreased, and only 12.39% had an increasing trend, while 23.46% of CWD districts decreased, mainly located in the upstream central region, and the increased area reached 76.54% and was widespread throughout the basin (Figure 4h). The areas with increasing trends in R10mm, R20mm, and R25mm accounted for 61.12%, 43.45%, and 34.78%, respectively, and were found in the upstream western, midstream southern, and downstream regions (Figure 4i–k). The areas with decreasing trends accounted for 38.88%, 56.55%, and 65.22%, respectively, and were concentrated in the upstream central.

In summary, from 2000 to 2020, extreme precipitation intensity, wet duration, and frequency increased in the upstream western (Tibetan Plateau) and downstream (Huang-Huai-Hai Plain), while a decreasing trend was observed in the typical temperate grassland area of the upstream central region and the typical temperate deciduous broadleaf forest area of the midstream.

3.1.3. Temporal Dynamics of the Extreme Temperature Indices

The annual cold extreme values were determined from the interannual variations in *ETI*s (Figure 5) and showed growth rates for TX10p and TN10p of 1.399 and 1.264 days/decade, respectively (Figure 5a). The annual warm extreme values exhibited growth rates for TX90p and TN90p of 0.868 days/decade and 2.403 days/decade, respectively (Figure 5b). This indicated a decline in the frequency of cold days and nights as well as warm days and nights. In terms of diurnal temperature changes, the change speed during cold days was slightly higher during the daytime than at night, while during warm days, the change speed at night was significantly faster than in the daytime. According to Figure 5c, the cold extreme values showed growth rates for TNn and TXn of 0.738 and 0.568 °C/decade, while the warm extreme values exhibited growth rates for TNx and TXx of 0.033 and 0.304 °C/decade, respectively. The decrease in speed at the daily maximum temperature was remarkably smaller than the increase in speed at the daily minimum temperature, indicating a trend towards convergence between the two extremes, which led to a slow decline in the DTR. The extreme temperature duration index, GSL, increased to 4.446 d/decade in the YRB (Figure 5e). The frost day (FD) occurrence and CSDI decrease rates were 5.529 and 0.800 days/decade, while the summer day (SU) occurrence and WSDI increase rates were 1.361 and 0.298 days/decade (Figure 5d,f). Considering the extreme temperature days and duration indices together, the decrease rate in the FD and cold days indices grew faster than the increase rate in the summer days and duration indices, indicating a continued rise in temperatures.

3.1.4. Spatial Evolution in Extreme Temperature Indices

Figure 6 shows that the proportions of TX10p and TN10p regions with an increasing trend reached 99.998% and 65.24%, respectively, while the values for decreasing regions were only 0.002% and 34.76%. The proportions of TX90p and TN90p regions with an increasing trend were as high as 71.62% and 96.37%, respectively, while the values for decreasing regions were only 28.38% and 3.63%. The areas with decreasing TNn and TXn values accounted for 63.88% and 90.70%, while the areas with increasing values accounted for 37.12% and 9.30%, respectively. The areas with decreasing TNx and TXx values accounted for 82.76% and 75.34%, while the areas with increasing values accounted for 17.24% and 24.66%, respectively. The areas with decreasing FD values accounted for 91.29%, while the increasing values reached 8.71%. The decreasing SU values accounted for 48.90%, while the areas with increasing values accounted for 51.10%. The expansion of areas with extreme cold and warm temperature values indicated a progressive growth in extreme temperatures (Figure 7a–j). The spatial trend of the DTR exhibited significant distribution differences, with the increase and decrease accounting for 54.74% and 45.26%, respectively.

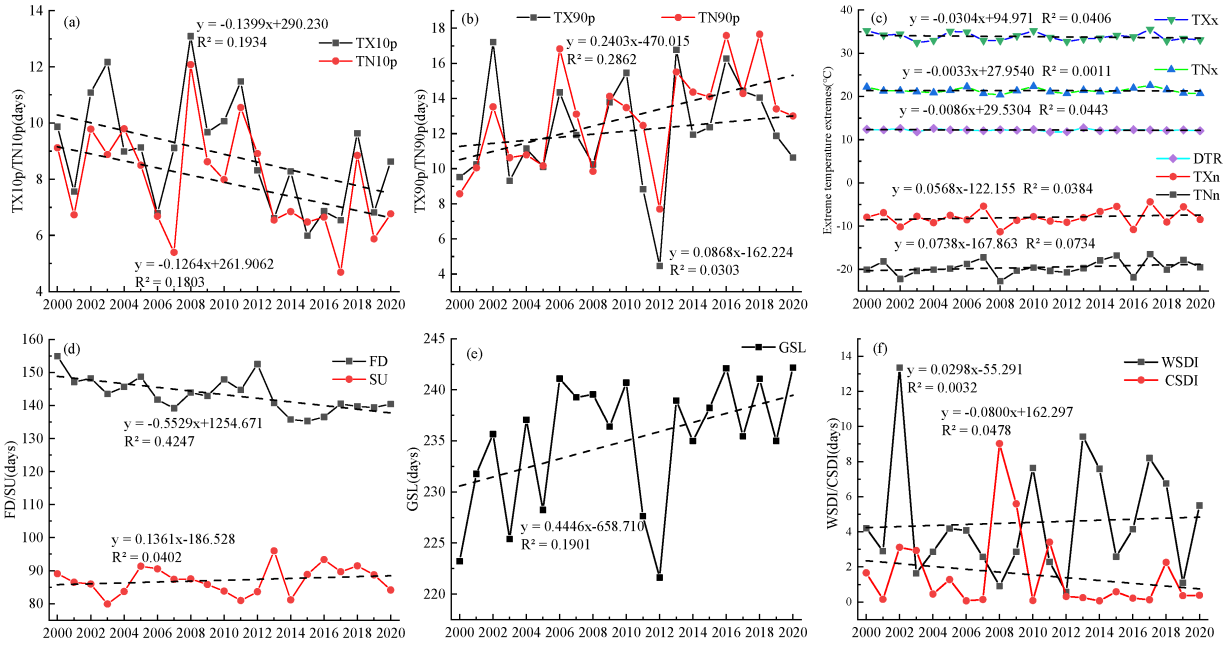

Figure 5. Temporal variations in the 14 extreme temperature indices (**a**–**f**). The black dotted line represents the trend of the variable during 2000–2020.

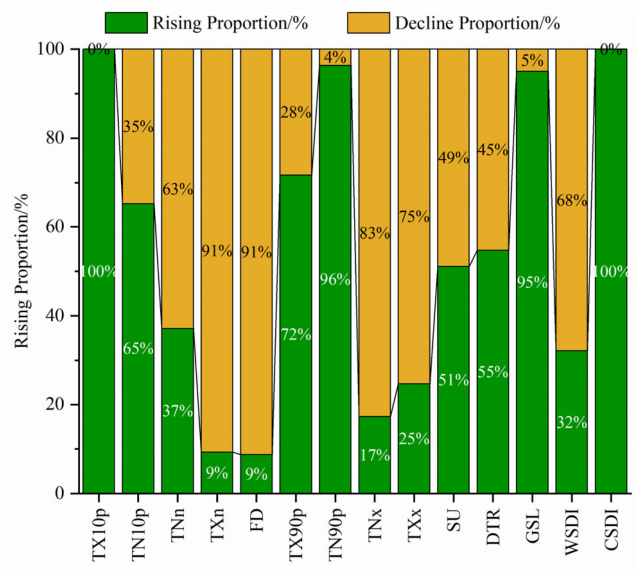

Figure 6. Area changes in the 14 extreme temperature indices during 2000–2020.

The area of declining DTR was primarily in the southwestern and northeastern portions of the upstream, while the regions with increased DTR were widely located in the mid-downstream (Figure 7k). The area with an increasing GSL reached 95.02%, with significant increases occurring in the north of the YRB and the Huang-Huai-Hai Plain in the downstream eastern region (Figure 7l). The decreasing WSDI reached 67.93%, while the area with an increasing value accounted for 32.07%. The area with an increasing CSDI reached 99.95%. Overall, the *ETI*s, in terms of temperature extremes, intensity, and duration, trended upward across most of the YRB during 2000–2020 (Figure 7).

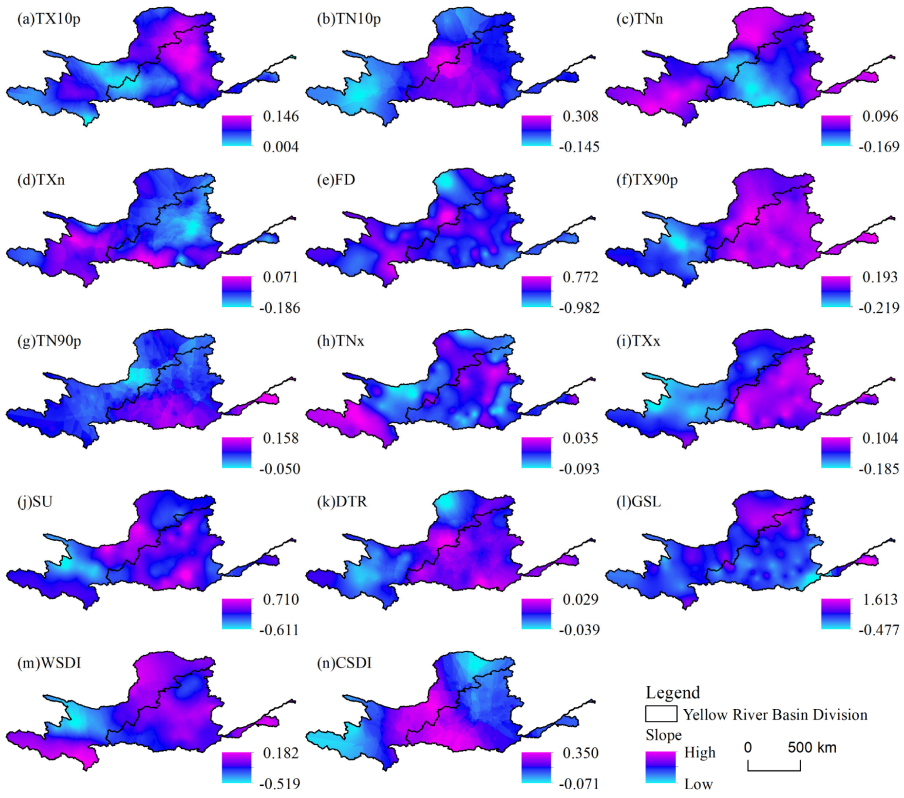

Figure 7. Spatial distribution of the 14 extreme temperature indices from 2000 to 2020 in YRB.

3.2. Spatiotemporal Changes in NDVI

By analyzing the NDVI trend in the YRB and its three major subbasins and comparing the differences in the NDVI trends among different subregions, the variations in vegetation activity in the area can be characterized. Figure 8 shows the trend of the annual average NDVI and its three major sub-basins from 2000 to 2020.

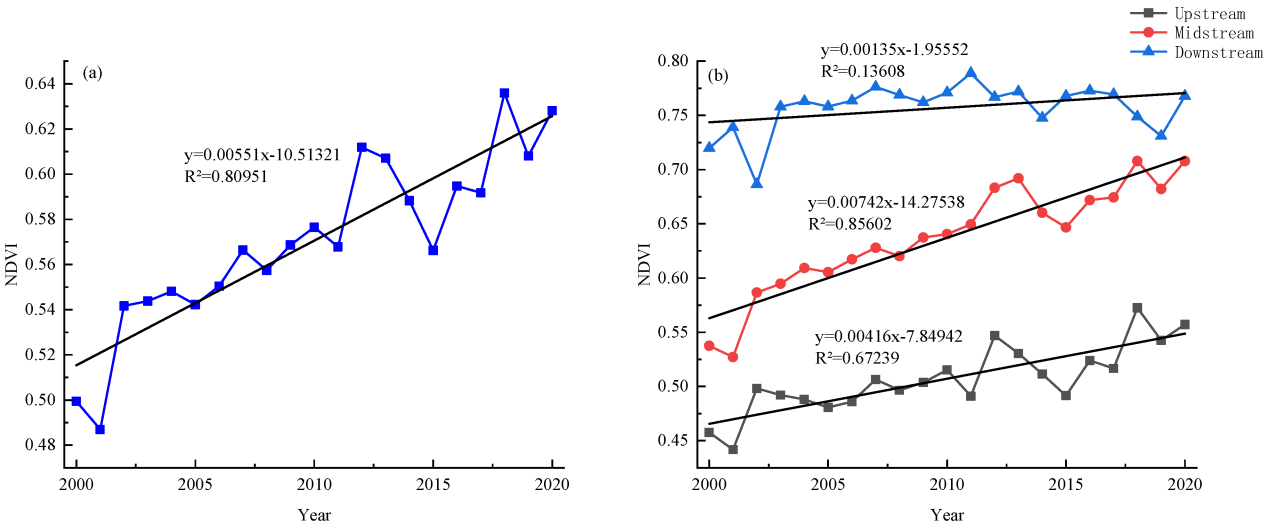

Figure 8. Trend of annual maximum NDVI changes in the (**a**) YRB and (**b**) three subbasins from 2000 to 2020.

The results indicated a remarkable growing trend of the NDVI with a rate of 0.055/decade during 2000–2020 (Figure 8a). The NDVI valley value of 0.487 occurred in 2001, while it peaked at 0.636 in 2018. Further investigation into the three major subbasins of the YRB

revealed that the trends of the NDVI in the upstream and midstream were consistent with the overall annual NDVI trend, showing a remarkable growth trend. The NDVI growth in the midstream was significantly higher than the overall trend, at a rate of 0.074/decade, indicating the significant effectiveness of vegetation restoration and management in this region. The NDVI growth rate upstream was 0.042/decade, which was slightly lower than the overall tread. Additionally, the vegetation downstream has maintained high coverage since 2000, with the slowest vegetation change rate in the past 21 years, at 0.013/decade (Figure 8b).

In terms of spatial distribution, the annual average NDVI values were higher in the west of the upstream, the central-southern regions of the midstream, and the downstream areas. However, they were lower in specific areas of the upstream, such as the high-altitude areas of the Tibetan Plateau, the Kubuqi Desert, and the MaoWusu Desert (Figure 9a). Concerning spatial change trends, the annual average NDVI demonstrated an overall growth trend, with improvement and degradation areas accounting for 87.33% and 12.63%, respectively (Figure 9b). The Loess Plateau region in the midstream of the YRB had remarkable growth, indicating notable success in ecological restoration of vegetation over the 21-year period. Conversely, areas facing severe degradation were primarily concentrated in the southern part of the midstream and downstream regions. This might be due to the high population density of the region, which made vegetation susceptible to influence from human activities. Additionally, urban expansion has transformed certain agricultural lands and grasslands into construction sites, leading to a certain degree of vegetation degradation. To promote ecological and environmental restoration, it will be necessary to intensify green vegetation construction efforts in these regions in the future.

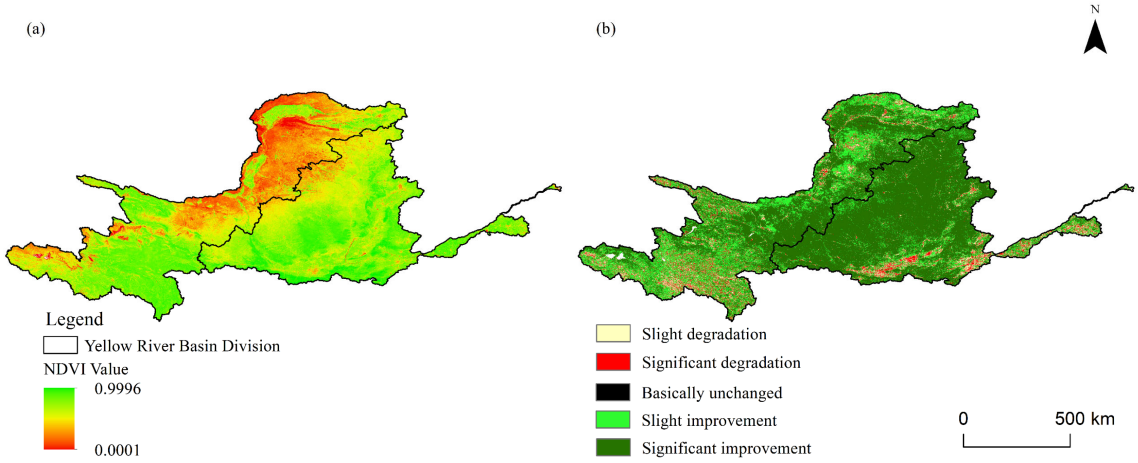

Figure 9. NDVI distribution and variation from 2000 to 2020 in the YRB. (**a**) Spatial distribution of the multi-year average annual NDVI; (**b**) spatial distribution of the significance level of the annual NDVI.

3.3. Uncovering the Major Factors Driving the NDVI Spatial Distribution

The results of factor detection have quantified the explanatory power of environmental variables for spatial variation in the NDVI. Figure 10 shows the weighted factors of the NDVI spatial variation for 2000, 2005, 2010, 2015, and 2020 and the average over 21 years. All factors passed the significance test. The results indicated that PRCPTOT, R10mm, CWD, and TXn were the dominant factors for the NDVI in each year, with *q*-values above 0.45. While PRCPTOT consistently maintained its dominant position, the other factors varied over time. The secondary driving factors for the NDVI are R95p, R99p, CDD, and Rx5day. Extreme precipitation has made a vital contribution to the spatial variation in the NDVI in the YRB in terms of intensity, frequency, and duration (Table 3), suggesting that precipitation is the most significant limiting element of vegetation distribution [44]. In addition, the *q* values of the six *ETI*s, TN10p, TX10p, WSDI, CSDI, TX90p, and TN90p, were all lower than 0.1, which indicated that the vegetation changes in the YRB were less responsive to the *ETI*s that were below the 10th percentile and at the upper 10th percentile.

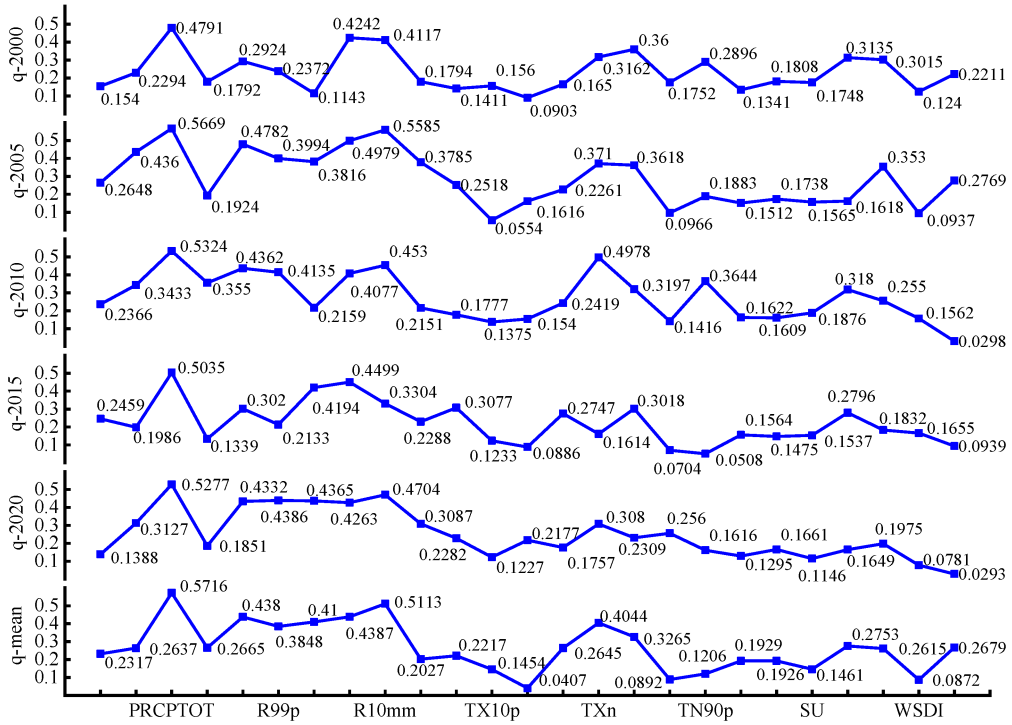

Figure 10. *q*-value changes of 25 extreme climate indices on NDVI in the YRB over 6 periods (2000, 2005, 2010, 2015, 2020, and overall mean).

Table 3. Changes in explanatory power (*q* values) in 2000, 2005, 2010, 2015, 2020, and the average of 21 years.

Year	2000	2005	2010	2015	2020	Average of 21 Years
Dominant factors	PRCPTOT	PRCPTOT R10mm CWD	PRCPTOT TXn R10mm	PRCPTOT	PRCPTOT R10mm	PRCPTOT R10mm
Secondary factors	CWD R10mm	R95p Rx5day	R95p R99p CWD	CWD CDD	R99p CDD R95p CWD	CWD R95p CDD

The interaction detector quantitatively identified the explanatory power and kinds of interactions between pairs of driving factors. Among the results from the five periods, the dominant types of interaction between two factors were bifactor enhancement and nonlinear enhancement. Table 4 summarizes the top five interactions for each period. The interaction between PRCPTOT and *ETI*s showed a bifactor enhancement effect, which significantly enhanced the influence of a single factor on the NDVI. Furthermore, in 2010, the interactions between R95p and TXn as well as between Rx5day and TXn had relatively large *q* values of 0.6025 and 0.5990, respectively. In 2015, CWD and R20mm had a *q* value of 0.5857. These results demonstrate the crucial role of the coordinated effects of water and heat on vegetation growth.

Table 4. Top five factor interactions for 5 periods (2000, 2005, 2010, 2015, and 2020).

Year	Rank of Interactive Explanatory Power (Top Five)
2000	PRCPTOT ∩ R20mm = 0.5969 ** > PRCPTOT ∩ TNx = 0.5962 ** > PRCPTOT ∩ SU = 0.5856 ** > PRCPTOT ∩ SDII = 0.5852 ** > PRCPTOT ∩ GSL = 0.5781 **
2005	PRCPTOT ∩ TNn = 0.6362 ** > PRCPTOT ∩ TN10p =0.6336 ** > PRCPTOT ∩TXx = 0.6259 ** > PRCPTOT ∩ TX90p = 0.6236 ** > PRCPTOT ∩ SDII = 0.6219 **
2010	PRCPTOT ∩ TXn = 0.6083 ** > PRCPTOT ∩ TX10p = 0.6052 ** > R95p ∩ TXn = 0.6025 ** > PRCPTOT ∩ R25mm = 0.6012 ** > Rx5day ∩ TXn = 0.5990 **
2015	PRCPTOT ∩ SU = 0.5930 ** > PRCPTOT ∩ TNx = 0.5877 ** > R95p ∩ TXx = 0.5868 ** > CWD∩ R20mm = 0.5857 ** > PRCPTOT ∩ TX90p = 0.5828 *
2020	PRCPTOT ∩ TNx = 0.5781 ** > PRCPTOT ∩ TXx = 0.5736 ** > PRCPTOT ∩ GSL = 0.5712 ** > PRCPTOT ∩ TX10p = 0.5678 ** > PRCPTOT ∩ FD = 0.5662 **

Note: "**" represents bifactor enhancement, and "*" represents nonlinear enhancement.

3.4. NDVI Response to Extreme Climate

The vegetation response to climate change may be more pronounced under extreme climate conditions. Existing research has also indicated a significant link between vegetation cover and ECE, especially in semiarid and arid regions. Therefore, there is a need to deeply explore the response mechanisms between ECEs and vegetation. Figures 11 and 12 show the Pearson correlation analysis results with the NDVI and raster images generated from the 25 extreme climate index data calculated by the RClimDex1.1 software for 86 meteorological stations after interpolation by kriging.

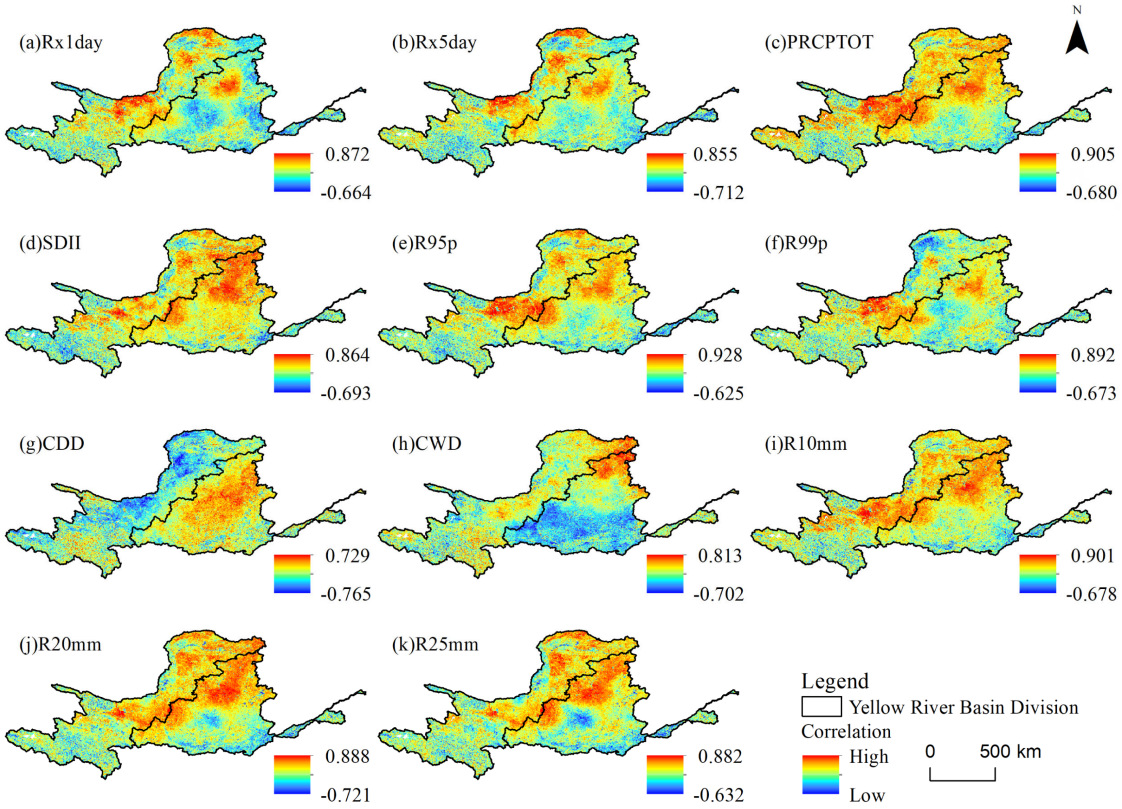

Figure 11. The correlation between the extreme precipitation indices and the annual NDVI during 2000–2020 in the YRB.

3.4.1. Correlation between Extreme Precipitation and NDVI

In terms of both intensity and frequency of extreme precipitation, the findings in Figure 11 indicates that the NDVI exhibited spatial patterns. Specifically, Figure 11a–f,i–k show that the NDVI was significantly and positively correlated with Rx1day, Rx5day, PRCPTOT, SDII, R95p, R99p, R10mm, R20mm, and R25mm in the middle and north regions of the upstream and midstream in the YRB ($p < 0.05$). Increased precipitation amounts and extreme precipitation helped alleviate the negative impacts of rising temperatures, thereby promoting rapid growth in vegetation cover. This result was consistent with the NDVI trend over the 21-year period (Figure 9) and supported the dominant influence of PRCPTOT on NDVI changes (Figure 10). The negative correlation between the NDVI and

Rx1day, Rx5day, PRCPTOT, SDII, R95p, R99p, R10mm, R20mm, and R25mm was mainly found in the upstream, western, and midstream southern regions, although the overall correlation was relatively weak.

In the midstream of the YRB, the NDVI and CDD were strongly positively correlated, while in the upstream, the NDVI and CDD were negatively correlated, forming a "stripe" along the boundary from southwest to northeast (Figure 11g). The NDVI and CWD exhibited a remarkable positive correlation in the northern regions, while a negative correlation was found in the south of the midstream (Figure 11h).

3.4.2. Correlation between Extreme Temperature and NDVI

Figure 12 presents the correlation analysis between 14 *ETI*s and the annual NDVI in the YRB, with significance levels obtained through statistical tests set at 0.05. TX10p was positively correlated with the NDVI in the upstream northeast region of the YRB, but the correlation was not significant. TX10p was negatively correlated with the NDVI, mainly in the midstream (Figure 12a). TN10p was remarkably positively correlated with the NDVI in the upstream northeastern region of the YRB and the midstream south-central region, while it was negatively correlated in the upstream western region (Figure 12b). The correlation between cold days and cold nights with the NDVI remained consistent in the western and northern regions. TX90p and TN90p exhibited a significantly positive correlation with the NDVI in the upstream southwestern and midstream central regions, while negative correlations were mainly found in the upstream northeastern region (Figure 12f,h).

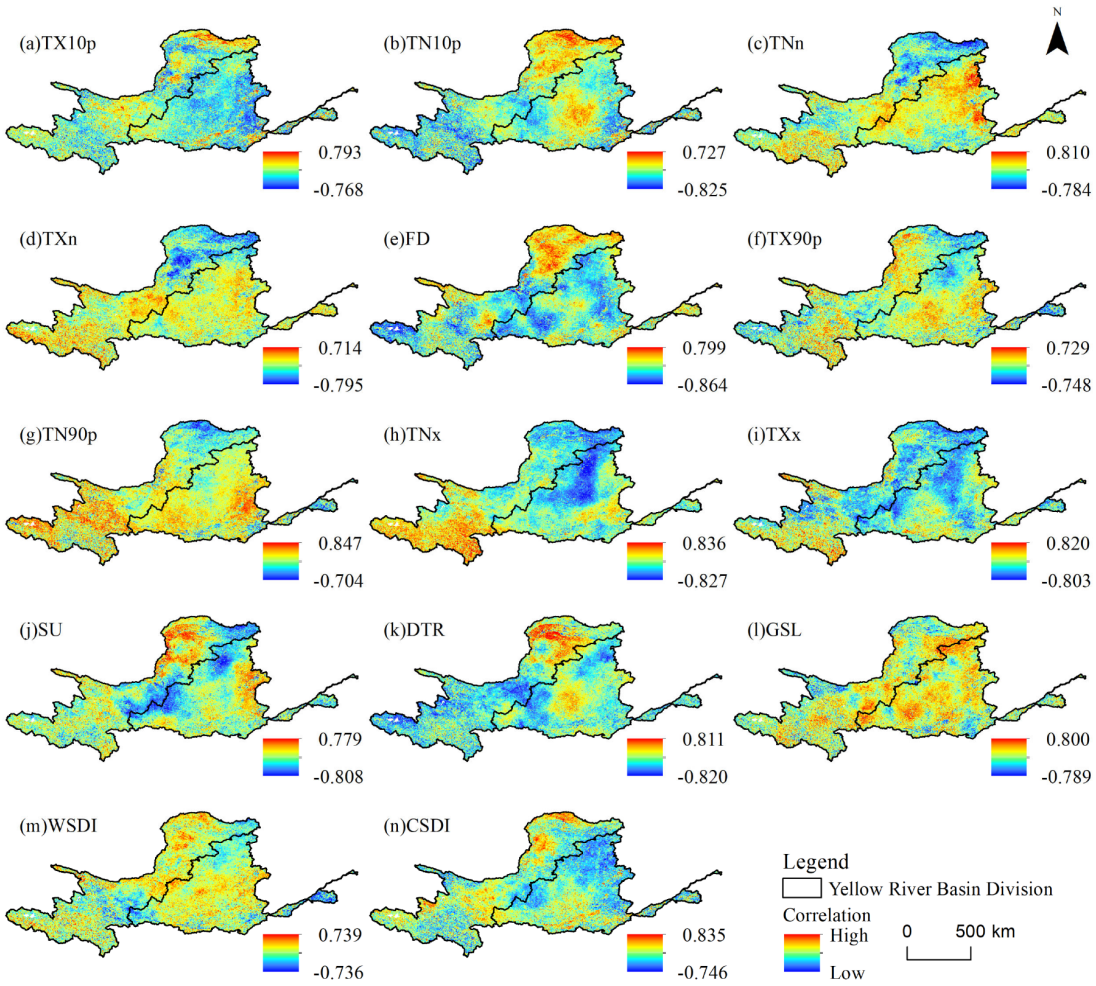

Figure 12. The correlation between the extreme temperature indices and the annual NDVI during 2000–2020 in the YRB.

In the upstream western and midstream central-southern regions of the YRB, the elevated quantity of warm days and nights helped maintain soil temperature and balance, mitigating the negative impacts of increased cold nights and enhancing vegetation's carbon fixation capacity, primary productivity, and respiration. The warming has created favorable conditions for vegetation growth. The increase in cold days and nights in the upstream northeastern region benefited soil moisture retention and reduced evapotranspiration, promoting vegetation growth in that area.

TNn and TXn exhibited a positive correlation with the NDVI in the upstream western region and the midstream, while in the upstream northeastern region, they were negatively correlated with the NDVI (Figure 12c,d). TNx and TXx were positively correlated with the NDVI in the upstream southwestern region of the YRB (Figure 12h,i). This study revealed that the vegetation-climate productivity potential of the region was positively influenced by temperature, with temperature being the dominant factor in this regard. Therefore, rising daily temperatures promoted vegetation growth in this area. TNx and TXx exhibited a highly negative correlation with the NDVI in the upstream northeastern region and the midstream middle-northern region, which may be due to the presence of desert areas and loess plateaus in these regions, combined with arid climates and poor water conditions (Figure 12h,i). The increase in daily temperature accelerated vegetation transpiration and soil moisture evaporation, negatively affecting vegetation growth to some extent. FD and SU were highly positively correlated with the NDVI, mainly in the upstream north-eastern region, and significantly negatively correlated with the NDVI at the upstream and downstream junctions (Figure 12e,j).

DTR was significantly positively correlated with the NDVI mainly in the upstream northeastern region and negatively correlated with the NDVI mainly in the upstream southwestern region and midstream (Figure 12k). The positive correlation of GSL with the NDVI was widely distributed in the upstream and midstream, and the negative correlation did not pass the test of significance (Figure 12l). The positive correlation of WSDI with the NDVI occurred mainly in the upstream eastern part and midstream south-central part, while the negative correlation of CSDI with the NDVI occurred mainly in the midstream north-central part (Figure 12m,n).

3.4.3. The Impacts of ECCs on NDVI for Various Vegetation Classes

From Figure 13, it was found that the highest positive correlation between *EPI*s and the NDVI occurs in grassland meadows, broadleaf forests, and shrub areas. The maximum positive correlations in these three regions were 0.772, 0.669, and 0.666, respectively, while the highest negative correlations were 0.609, 0.582, and 0.489. Among the correlations, the impacts of PRCPTOT and CDD on the NDVI were the most significant. The extreme temperature index TXn exhibited the highest positive correlation with the NDVI in the three major regions, with values of 0.598, 0.645, and 0.632. Correspondingly, the highest negative correlations were 0.67, 0.47, and 0.408, where the influence of CSDI on the NDVI was relatively important. However, in desert and cultivated vegetation areas, the correlation between changes in *EPI*s, *ETI*s, and the NDVI was relatively low. This is due to the lower vegetation coverage in deserts, where vegetation changes are less affected by environmental variations. On the other hand, cultivated vegetation was actively managed within the scope of human activities, leading to reduced natural impacts on vegetation.

Viewed from the perspectives of both extreme precipitation and extreme temperature, the former generally exhibited a higher correlation with the NDVI. Table 4 also supports the dominant role of *EPI*s in influencing vegetation. With the exception of CDD, most *EPI*s demonstrated positive correlations with the NDVI, while, apart from TXn, TX90p, and TN90p, *ETI*s were generally negatively correlated with the NDVI. Moreover, the interaction between *EPI*s and *ETI*s strengthened the impact of individual factors on vegetation, aligning with the dominance of the PRCPTOT-TXn dual-factor influence on vegetation changes in 2010, as indicated in Table 4.

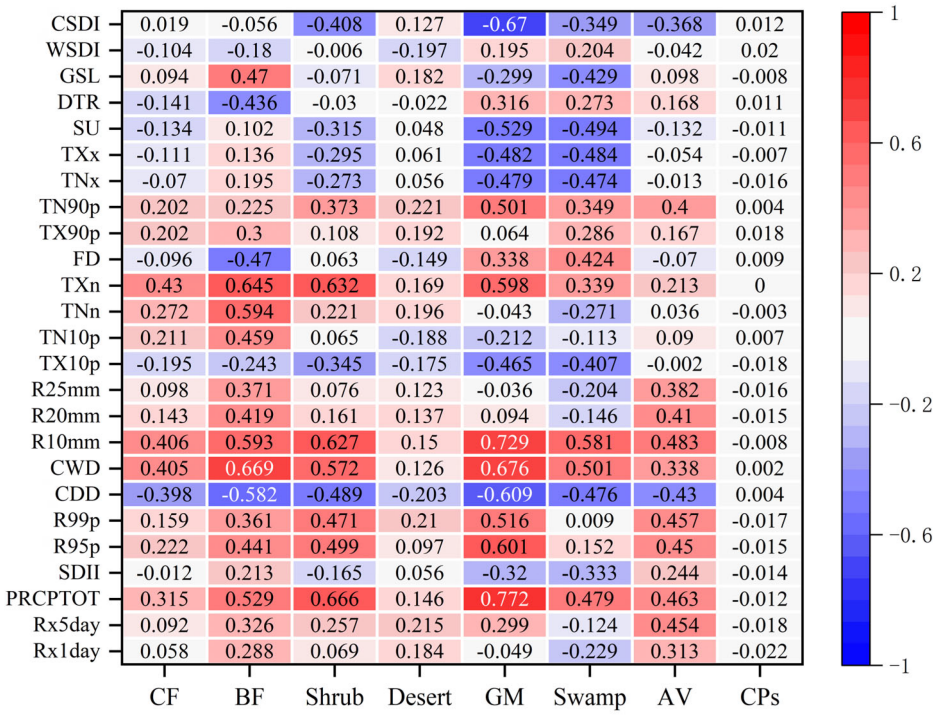

Figure 13. The correlation between ECC and the NDVI of different plant types during 2000–2020 in the YRB. Abbreviations: alpine vegetation (AV); broadleaf forest (BF); coniferous forest (CF); cultivated plants (CPs); grassland and meadow (GM).

4. Discussion

4.1. Model Fitting and Illustrations

To monitor the dynamic interplay and spatial scale effects between vegetation and extreme climate change, this study employed regression analysis, linking extreme climate indices with the NDVI. Following multicollinearity assessments, variables meeting two criteria (VIF < 10 and factor detection *q*-values) were chosen for localized modeling. The different model results are depicted in Table 5. All parameter estimation values exhibit *p* values lower than 0.1. Enhanced adjusted R^2 alongside diminished AICc values signifies improved model performance [45]. Out of the five study periods, the OLS model showed the lowest adjusted R^2 and the highest AICc. This could be attributed to the omission of inherent spatial heterogeneity between the NDVI and ECI in the model, culminating in biased estimations. In contrast to global models, both local models, GWR and MGWR, achieved more favorable regression outcomes. GWR accounted for spatial heterogeneity and local characteristics, resulting in a goodness of fit R^2 surpassing 0.7 (Table 5). Nevertheless, it constrained all explanatory variables to a uniform fixed bandwidth, thereby failing to portray the distinct spatial scale impacts of each variable in their individual spatial processes. Hence, spatial variation is not accurately depicted. Conversely, MGWR permitted distinct extreme climate indices to encompass varied spatial smoothing levels, engaging in localized modeling across diverse spatial scales to pinpoint optimal geographical modeling scales. Consequently, in comparison to GWR, the MGWR results reveal an escalation in adjusted R^2 coupled with a reduction in AICc. Figure 14 portrays the standard residuals of MGWR for the five study periods, commonly depicting a stochastic spatial dispersion pattern. Additionally, the absolute residuals across all regions remain under 2.5, signifying that the local model is robust and the results are reliable [46].

Table 5. Comparison of the fitting measures for the OLS, GWR, and MGWR models.

Year	OLS		GWR		MGWR	
	Adj.R^2	**AICc**	**Adj.R^2**	**AICc**	**Adj.R^2**	**AICc**
2000	0.485	9404.078	0.705	7610.028	0.761	5441.652
2005	0.535	9487.666	0.776	7298.727	0.740	5726.879
2010	0.495	9819.916	0.755	7588.276	0.765	5361.018
2015	0.478	9776.743	0.737	7707.585	0.767	5346.585
2020	0.493	9119.293	0.704	7610.028	0.725	5954.629

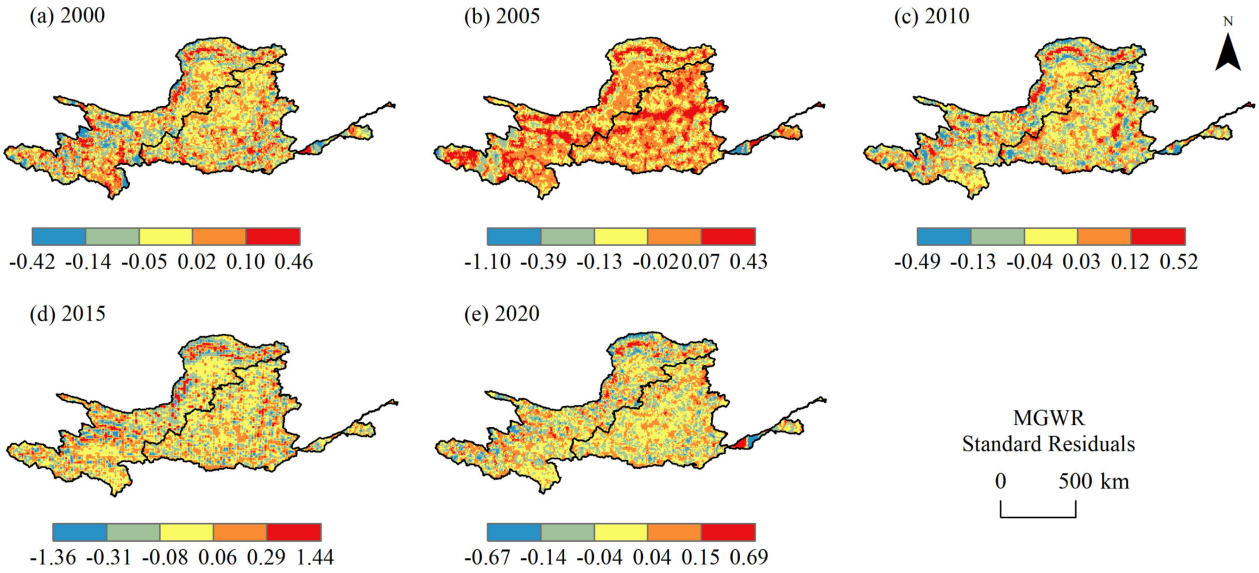

Figure 14. The spatial distribution of the MGWR standard residuals from 2000 to 2020. (**a**) Phase 1, 2000; (**b**) Phase 2, 2005; (**c**) Phase 3, 2010; (**d**) Phase 4, 2015; (**e**) Phase 5, 2020.

4.2. The Impact of Extreme Climate Change on Vegetation

We successfully carried out a spatiotemporal and driver analysis of 25 extreme climate indices and the NDVI for the same period. Our findings highlighted a noteworthy upsurge in the NDVI of the YRB from 2000 to 2020 (0.055/decade), aligning with earlier research [47]. This is consistent with the results of the trend analysis of 1 km of NDVI data after the assimilation of machine learning methods [48]. This growth rate surpasses China's rate (0.03/decade, 1998–2017) [49] and Northern China's rate (0.01/decade, 1982–2018) [50]. Regarding changes in extreme climate indices, our results unveiled prominent escalating tendencies for *EPI*s Rx1day, Rx5day, PRCPTOT, R95p, R99p, and R10mm (1.910 mm/decade, 5.535 mm/decade, 45.846 mm/decade, 20.742 mm/a, and 6.999 mm/a). Similarly, the *ETI*s TX90p, TN90p, TNn, TXn, SU, and GSL also manifest noteworthy increasing patterns (0.868 days/decade, 2.403/decade, 0.738 °C/decade, 0.568 °C/decade, 1.361 days/decade, and 4.446 days/decade, respectively). These outcomes align with those of previous investigations [48].

Examining the link between *ECI*s and vegetation cover can contribute to the identification of ecosystems that are susceptible to extreme climate conditions. Our findings showed noteworthy positive correlations ($p < 0.05$) between the NDVI, PRCPTOT, and R10mm. This is consistent with the increasing trend of the extreme temperature index, which was obtained in Inner Mongolia using multiple linear regression and full subset regression. This was in accordance with the findings in the middle and lower reaches of the Yangtze River in China [37], Pakistan [51], and global drylands [52], which have shown that variation in extreme precipitation intensity has been consistent with or significantly influenced vegetation activities. On the continental scale, a strong connection between extreme precipitation and average precipitation was found for Australia [53]. Over land,

the wettest day of all seasons was found to intensify strongly during the monsoon in the middle and high latitudes of the Northern Hemisphere. Additionally, the intensity of extreme precipitation was forecast to increase alongside elevated mean precipitation across all seasons throughout the 21st century [54]. As the frequency of extreme precipitation increased, R20mm and R25mm displayed a remarkable negative correlation with the NDVI, suggesting that increased precipitation might enhance vegetation growth by supplementing soil moisture [52]. In the upstream of the YRB, CDD was broadly negatively correlated with the NDVI, especially in grassland meadows (−0.609) and deserts (−0.203). On the contrary, in the coniferous and broadleaf forests of the Loess Plateau, the significantly positive correlation coefficients between CWD and the NDVI were 0.405 and 0.669, respectively. Furthermore, R99p displayed a less pronounced correlation with the NDVI when contrasted with R95p. Collectively, these findings indicated that excessive extreme precipitation could impede vegetation growth due to elevated soil moisture content and soil erosion, resulting in an unfavorable environment for vegetation development [55]. Additionally, damp conditions caused by precipitation have been found to diminish solar radiation absorption, resulting in decreased temperatures and soil saturation, which acts as a restricting factor for vegetation growth [56].

Intriguingly, the present research uncovered a divergence in the effects of warm and cold extreme values on vegetation with the NDVI. This is because vegetation types such as coniferous forests, broadleaf forests, and grassland meadows flourish in temperature conditions that are relatively well suited. This enables them to enhance photosynthesis by effectively harnessing solar radiation and providing the necessary thermal conditions for vegetation growth [21]. However, coniferous forests are vulnerable to severe frost events [57], leading to a diminished correlation with the NDVI during episodes of extreme cold temperatures. TN90p displayed a noteworthy positive correlation ($p < 0.05$) with the NDVI, which is especially conspicuous in grassland meadows and shrub regions. This can be attributed to the comparatively reduced sensitivity of herbaceous plants to extreme damp and cold conditions, enabling their survival even on chillier nights [58]. Importantly, extreme warmth can induce soil desiccation, diminishing the water usage capacity of plants [59]. Desert vegetation, which depends on its ability to withstand drought, and high-altitude vegetation, which relies on cold resilience, exhibit reduced correlations with both cold and warm extreme values [60,61]. Cultivated plants do not demonstrate any substantial adverse effects from either type of extreme value. Furthermore, our study reveals markedly unfavorable correlations involving grassland meadows, marshes, and extreme events of low temperatures (TNx, TXx, and SU). The injurious effects of extreme cold temperatures on plant roots and tissues hinder the development of vegetation throughout the majority of the YRB [62]. For example, the correlation between cold extreme values (TX10p and TN10p) and warm extreme values (TX90p and TN90p) with the NDVI exhibits a complete reversal within the YRB. Similarly, TNn and YXn displayed inverse correlations with TNx and TXx, except for the upstream northern region, where the correlation turned negative. This discrepancy implied distinct effects of these indices on vegetation across different regions (Figure 12). Among the eight vegetation types, TXn exhibited a notable positive correlation ($p < 0$).

4.3. Limitations and Uncertainty

The limitations and unpredictability involved in analyzing the effects of ECC on vegetation are crucial and should not be disregarded. First, uncertainties stem from the data sources. While this study utilized a maximum synthesis approach to produce annual NDVI data, it is essential not to overlook the potential impact of clouds and haze on remote sensing data [63,64]. Clouds and haze can affect the data acquisition and quality of parameters such as infrared and near-infrared bands, thus reducing the accuracy of the NDVI. Additionally, during the resampling process, the uniformity of spatial resolution may influence the precision of research outcomes [65,66]. Consequently, uncertainties inherent in the data could potentially impact the reliability of this investigation.

Second, the significance of the discreteness of meteorological station observation data should not be overlooked. The kriging interpolation method, commonly associated with spatial weather station data, are used to scrutinize the effect of natural factors on alterations in vegetation [67,68]. Nevertheless, distinct interpolation approaches yield varying outcomes, introducing elements of uncertainty. In this study, the Kriging interpolation method was used to interpolate the extreme climate index data from spatially neighboring stations, while the spline interpolation method was utilized to interpolate the continuous data via fitting to a smooth surface. The latter can improve the interpolation accuracy for regions with uneven station distribution, such as the Kubuzi Desert, Loess Plateau, and lower Yellow River.

Moreover, the impacts of HA on vegetation and CC, frequently attributed solely to climatic factors, are often disregarded. Urban expansion directly affects the regional distribution of vegetation and indirectly affects the climate. For instance, the urban heat island effect leads to climatic warming [69,70] and increases the demand for water resources. However, vegetation is caught in a water scarcity crisis due to the interaction between urbanization and the increasing trend of extreme warmth indices TN90p and TX90p. In addition, urbanization coupled with long-lived greenhouse gases (LLGHG) exacerbates extreme precipitation both in terms of quantity and frequency [71,72]. Extreme precipitation indices of Rx5day, R95p, and R10mm had a significant upward trend, possibly leading to flooding disasters, exacerbation of soil erosion, and deterioration of the vegetation growth environment. This research solely investigated the influence of ECC on YRBs vegetation. In the future, a comprehensive exploration of the factors influencing vegetation should encompass both natural and human-induced disruptions. Additionally, the investigation of the link between the NDVI and specific ECEs, such as flash drought, merits future consideration.

5. Conclusions

The research demonstrated that the NDVI in the YRB revealed a notable growing trend, increasing at a rate of 0.055/decade. Notably, the midstream region displayed the most rapid growth, at a rate of 0.074 per decade. In contrast, the upstream and downstream regions showed growth rates lower than the overall rate of the YRB. Moreover, the annual NDVI exhibited an overall upward trend, with areas of enhancement constituting 87.33% and areas of decline accounting for 12.63%. The outcomes of the geographical detector analysis indicated that precipitation (PRCPTOT) primarily affects vegetation. The combined effects of hydrothermal conditions play a pivotal role in promoting vegetation growth. Various vegetation types exhibit substantial variations in their responsiveness to water, with grassland meadows demonstrating higher sensitivity than woody plants. Desert vegetation and cultivated plants exhibit the weakest reaction to precipitation. Furthermore, apart from CDD and SDII, indices of extreme precipitation exerted positive influences on the NDVI. Cold temperature extreme events (TXn, TNn, and TN10p) exhibited a notable positive correlation with the NDVI, surpassing the influence of other extreme temperature events. Regarding diverse vegetation categories, fluctuations in the NDVI among grassland meadows, broadleaf forests, and shrubs were connected to extreme precipitation indices (PRCPTOT, R95p, R99p, CWD, and R10mm) as well as extreme temperature (TXn). In contrast, desert vegetation and cultivated plants displayed a comparatively modest reaction to extreme climatic incidents. The findings suggested that, within the Yellow River basin, extreme precipitation events exert a more substantial influence on vegetation than extreme temperature events. Hence, the interplay between temperature and precipitation should not be underestimated. These findings contribute to a holistic comprehension of the role played by different climate alterations in shaping the behavior of arid vegetation. In subsequent research, a more thorough investigation of extreme climate events should be prioritized to mitigate their detrimental impacts on vegetation. This endeavor is of paramount significance for the restoration of arid ecosystems.

Author Contributions: Conceptualization, H.X., Z.L. and G.D.; methodology, H.X., Z.L., G.D. and X.L.; software, Z.L. and X.L.; formal analysis, H.X., Z.L. and G.D.; data curation, Z.L.; writing-original draft, Z.L.; writing-review and editing, H.X., G.D. and Y.L.; visualization, Z.L. and X.L.; funding acquisition, H.X. and G.D. All authors have read and agreed to the published version of the manuscript.

Funding: This research was funded by grants received by Guotao Dong from the National Natural Science Foundation of China (grant number 51779099), by Huazhu Xue from the Key Scientific and Technological Project of Henan Province (232102320247), by Huazhu Xue from the Fundamental Research Funds for the Universities of Henan Province (NSFRF230631), and by Yaokang Lian from the Special Funding for Young Talents in Longyuan of Gansu Province.

Data Availability Statement: MOD13Q1 used in this paper can be downloaded from the Google Earth Engine. Precipitation and temperature data were selected from the National Meteorological Science Data Center. The URLs of the data sources are given in Section 2.2 (Data sources and processing). All data are from public datasets.

Conflicts of Interest: The authors declare no conflicts of interest.

References

1. Stott, P. How climate change affects extreme weather events Research can increasingly determine the contribution of climate change to extreme events such as droughts. *Science* **2016**, *352*, 1517–1518. [CrossRef] [PubMed]
2. Ning, G.C.; Luo, M.; Zhang, W.; Liu, Z.; Wang, S.G.; Gao, T. Rising risks of compound extreme heat-precipitation events in China. *Int. J. Climatol.* **2022**, *42*, 5785–5795. [CrossRef]
3. Otto, C.; Piontek, F.; Kalkuhl, M.; Frieler, K. Event-based models to understand the scale of the impact of extremes. *Nat. Energy* **2020**, *5*, 111–114. [CrossRef]
4. Ummenhofer, C.C.; Meehl, G.A. Extreme weather and climate events with ecological relevance: A review. *Philos. Trans. R. Soc. Lond. B Biol. Sci.* **2017**, *372*, 20160135. [CrossRef] [PubMed]
5. Nangombe, S.S.; Zhou, T.; Zhang, W.; Zou, L.; Li, D. High-Temperature Extreme Events over Africa under 1.5 and 2 °C of Global Warming. *J. Geophys. Res.* **2019**, *124*, 4413–4428. [CrossRef]
6. AghaKouchak, A.; Chiang, F.; Huning, L.S.; Love, C.A.; Mallakpour, I.; Mazdiyasni, O.; Moftakhari, H.; Papalexiou, S.M.; Ragno, E.; Sadegh, M. Climate Extremes and Compound Hazards in a Warming World. *Annu. Rev. Earth Planet. Sci.* **2020**, *48*, 519–548. [CrossRef]
7. Chen, X.X.; Wang, L.C.; Niu, Z.G.; Zhang, M.; Li, C.A.; Li, J.R. The effects of projected climate change and extreme climate on maize and rice in the Yangtze River Basin, China. *Agric. For. Meteorol.* **2020**, *282*, 107867. [CrossRef]
8. Costa, A.A.; Guimarães, S.O.; Sales, D.C.; das Chagas Vasconcelos Junior, F.; Marinho, M.W.S.; Pereira, J.M.R.; Martins, E.S.P.R.; da Silva, E.M. Precipitation extremes over the tropical Americas under RCP4.5 and RCP8.5 climate change scenarios: Results from dynamical downscaling simulations. *Int. J. Climatol.* **2022**, *43*, 787–803. [CrossRef]
9. Zhu, X.; Lee, S.Y.; Wen, X.H.; Ji, Z.M.; Lin, L.; Wei, Z.G.; Zheng, Z.Y.; Xu, D.Y.; Dong, W.J. Extreme climate changes over three major river basins in China as seen in CMIP5 and CMIP6. *Clim. Dyn.* **2021**, *57*, 1187–1205. [CrossRef]
10. Wuebbles, D.; Meehl, G.; Hayhoe, K.; Karl, T.R.; Kunkel, K.; Santer, B.; Wehner, M.; Colle, B.; Fischer, E.M.; Fu, R.; et al. CMIP5 CLIMATE MODEL ANALYSES Climate Extremes in the United States. *Bull. Am. Meteorol. Soc.* **2014**, *95*, 571–583. [CrossRef]
11. Ridder, N.N.; Ukkola, A.M.; Pitman, A.J.; Perkins-Kirkpatrick, S.E. Increased occurrence of high impact compound events under climate change. *NPJ Clim. Atmos. Sci.* **2022**, *5*, 3. [CrossRef]
12. Fischer, E.M.; Sippel, S.; Knutti, R. Increasing probability of record-shattering climate extremes. *Nat. Clim. Chang.* **2021**, *11*, 689–695. [CrossRef]
13. Wu, J.; Han, Z.Y.; Xu, Y.; Zhou, B.T.; Gao, X.J. Changes in Extreme Climate Events in China Under 1.5 degrees C-4 degrees C Global Warming Targets: Projections Using an Ensemble of Regional Climate Model Simulations. *J. Geophys. Res.* **2020**, *125*, e2019JD031057. [CrossRef]
14. Meng, X.Y.; Gao, X.; Li, S.Y.; Lei, J.Q. Spatial and Temporal Characteristics of Vegetation NDVI Changes and the Driving Forces in Mongolia during 1982-2015. *Remote Sens.* **2020**, *12*, 603. [CrossRef]
15. Huang, S.; Tang, L.N.; Hupy, J.P.; Wang, Y.; Shao, G.F. A commentary review on the use of normalized difference vegetation index (NDVI) in the era of popular remote sensing. *J. For. Res.* **2021**, *32*, 1–6. [CrossRef]
16. Neinavaz, E.; Skidmore, A.K.; Darvishzadeh, R. Effects of prediction accuracy of the proportion of vegetation cover on land surface emissivity and temperature using the NDVI threshold method. *Int. J. Appl. Earth Obs. Geoinf.* **2020**, *85*, 101984. [CrossRef]
17. Shah, I.A.; Muhammad, Z.; Khan, H. Impact of climate change on spatiotemporal variations in the vegetation cover and hydrology of district Nowshera. *J. Water Clim. Chang.* **2022**, *13*, 3867–3882. [CrossRef]
18. Liu, Q.; Yao, F.M.; Garcia-Garcia, A.; Zhang, J.H.; Li, J.; Ma, S.Y.; Li, S.J.; Peng, J. The response and sensitivity of global vegetation to water stress: A comparison of different satellite-based NDVI products. *Int. J. Appl. Earth Obs. Geoinf.* **2023**, *120*, 103341. [CrossRef]

19. Meng, N.; Wang, N.A.; Cheng, H.Y.; Liu, X.; Niu, Z.M. Impacts of climate change and anthropogenic activities on the normalized difference vegetation index of desertified areas in northern China. *J. Geogr.* **2023**, *33*, 483–507. [CrossRef]
20. Wang, H.F.; Kang, C.Y.; Tian, Z.X.; Zhang, A.B.; Cao, Y. Vegetation periodic changes and relationships with climate in Inner Mongolia Based on the VMD method. *Ecol. Indic.* **2023**, *146*, 109764. [CrossRef]
21. Luo, M.; Sa, C.L.; Meng, F.H.; Duan, Y.C.; Liu, T.; Bao, Y.H. Assessing extreme climatic changes on a monthly scale and their implications for vegetation in Central Asia. *J. Clean. Prod.* **2020**, *271*, 122396. [CrossRef]
22. Cheng, Y.; Zhang, L.J.; Zhang, Z.Q.; Li, X.Y.; Wang, H.Y.; Xi, X. Spatiotemporal Variation and Influence Factors of Vegetation Cover in the Yellow River Basin (1982–2021) Based on GIMMS NDVI and MOD13A1. *Water* **2022**, *14*, 3274. [CrossRef]
23. Yang, T.; Wang, X.Y.; Yu, Z.B.; Krysanova, V.; Chen, X.; Schwartz, F.W.; Sudicky, E.A. Climate change and probabilistic scenario of streamflow extremes in an alpine region. *J. Geophys. Res.* **2014**, *119*, 8535–8551. [CrossRef]
24. Liu, K.; Yang, S.W.; Zhou, Q.; Qiao, Y.R. Spatiotemporal Evolution and Spatial Network Analysis of the Urban Ecological Carrying Capacity in the Yellow River Basin. *Int. J. Environ. Res. Public Health* **2022**, *19*, 229. [CrossRef] [PubMed]
25. Sun, S.Q.; Lue, Y.H.; Fu, B.H. Relations between physical and ecosystem service flows of freshwater are critical for water resource security in large dryland river basin. *Sci. Total Environ.* **2023**, *857*, 159549. [CrossRef] [PubMed]
26. Zhao, G.J.; Tian, P.; Mu, X.M.; Jiao, J.Y.; Wang, F.; Gao, P. Quantifying the impact of climate variability and human activities on streamflow in the middle reaches of the Yellow River basin, China. *J. Hydrol.* **2014**, *519*, 387–398. [CrossRef]
27. Niu, Z.G.; Feng, L.; Chen, X.X.; Yi, X.P. Evaluation and Future Projection of Extreme Climate Events in the Yellow River Basin and Yangtze River Basin in China Using Ensembled CMIP5 Models Data. *Int. J. Environ. Res. Public Health* **2021**, *18*, 6029. [CrossRef] [PubMed]
28. Li, J.; Xi, M.F.; Pan, Z.W.; Liu, Z.Z.; He, Z.L.; Qin, F. Response of NDVI and SIF to Meteorological Drought in the Yellow River Basin from 2001 to 2020. *Water* **2022**, *14*, 2978. [CrossRef]
29. Narasimhan, R.; Stow, D. Daily MODIS products for analyzing early season vegetation dynamics across the North Slope of Alaska. *Remote Sens. Environ.* **2010**, *114*, 1251–1262. [CrossRef]
30. Tian, J.Q.; Zhu, X.L.; Chen, J.; Wang, C.; Shen, M.G.; Yang, W.; Tan, X.Y.; Xu, S.; Li, Z.L. Improving the accuracy of spring phenology detection by optimally smoothing satellite vegetation index time series based on local cloud frequency. *ISPRS J. Photogramm. Remote Sens.* **2021**, *180*, 29–44. [CrossRef]
31. Sharma, S.; Saha, A.K. Statistical analysis of rainfall trends over Damodar River basin, India. *Arab. J. Geosci.* **2017**, *10*, 319. [CrossRef]
32. Zhang, X.; Zwiers, F.W. Comment on "Applicability of prewhitening to eliminate the influence of serial correlation on the Mann-Kendall test" by Sheng Yue and Chun Yuan Wang. *Water Resour. Res.* **2004**, *40*, W03805. [CrossRef]
33. Tosunoglu, F.; Kisi, O. Trend Analysis of Maximum Hydrologic Drought Variables Using Mann-Kendall and Sen's Innovative Trend Method. *River Res. Appl.* **2017**, *33*, 597–610. [CrossRef]
34. Rusciano, E.; Belbéoch, M.; Turpin, V.; Kramp, M.; Jiang, L.; Lizé, A.; Krieger, M. Odyssey Project: Contributing Actively to the Implementation of the Global Ocean Observing System. *Mar. Technol. Soc. J.* **2022**, *56*, 132–133. [CrossRef]
35. Wang, J.F.; Xu, C.D. Geodetector: Principle and prospective. *Acta Geol. Sin.* **2017**, *72*, 116–134.
36. Song, Y.Z.; Wang, J.F.; Ge, Y.; Xu, C.D. An optimal parameters-based geographical detector model enhances geographic characteristics of explanatory variables for spatial heterogeneity analysis: Cases with different types of spatial data. *GISci. Remote Sens.* **2020**, *57*, 593–610. [CrossRef]
37. Cui, L.F.; Wang, L.C.; Qu, S.; Singh, R.P.; Lai, Z.P.; Yao, R. Spatiotemporal extremes of temperature and precipitation during 1960–2015 in the Yangtze River Basin (China) and impacts on vegetation dynamics. *Theor. Appl. Climatol.* **2019**, *136*, 675–692. [CrossRef]
38. Zhao, W.; Yu, X.B.; Jiao, C.C.; Xu, C.D.; Liu, Y.; Wu, G.N. Increased association between climate change and vegetation index variation promotes the coupling of dominant factors and vegetation growth. *Sci. Total Environ.* **2021**, *767*, 144669. [CrossRef] [PubMed]
39. Li, M.L.; Yan, Q.W.; Li, G.E.; Yi, M.H.; Li, J. Spatio-Temporal Changes of Vegetation Cover and Its Influencing Factors in Northeast China from 2000 to 2021. *Remote Sens.* **2022**, *14*, 5720. [CrossRef]
40. Li, Z.; Huffman, T.; McConkey, B.; Townley-Smith, L. Monitoring and modeling spatial and temporal patterns of grassland dynamics using time-series MODIS NDVI with climate and stocking data. *Remote Sens. Environ.* **2013**, *138*, 232–244. [CrossRef]
41. Sawut, R.; Li, Y.; Kasimu, A.; Ablat, X. Examining the spatially varying effects of climatic and environmental pollution factors on the NDVI based on their spatially heterogeneous relationships in Bohai Rim, China. *J. Hydrol.* **2023**, *617*, 128815. [CrossRef]
42. Liu, H.M.; Huang, B.; Gao, S.H.; Wang, J.; Yang, C.; Li, R.R. Impacts of the evolving urban development on intra-urban surface thermal environment: Evidence from 323 Chinese cities. *Sci. Total Environ.* **2021**, *771*, 144810. [CrossRef]
43. Rong, Y.J.; Li, K.; Guo, J.W.; Zheng, L.F.; Luo, Y.; Yan, Y.; Wang, C.X.; Zhao, C.L.; Shang, X.; Wang, Z.T. Multi-scale spatio-temporal analysis of soil conservation service based on MGWR model: A case of Beijing-Tianjin-Hebei, China. *Ecol. Indic.* **2022**, *139*, 108946. [CrossRef]
44. He, L.; Guo, J.B.; Jiang, Q.O.; Zhang, Z.Y.; Yu, S.P. How did the Chinese Loess Plateau turn green from 2001 to 2020? An explanation using satellite data. *Catena* **2022**, *214*, 106246. [CrossRef]
45. Fotheringham, A.S.; Yang, W.; Kang, W. Multiscale geographically weighted regression (MGWR). *Ann. Am. Assoc. Geogr.* **2017**, *107*, 1247–1265. [CrossRef]

46. Mansour, S.; Al Kindi, A.; Al-Said, A.; Al-Said, A.; Atkinson, P. Sociodemographic determinants of COVID-19 incidence rates in Oman: Geospatial modelling using multiscale geographically weighted regression (MGWR). *Sustain. Cities Soc.* **2021**, *65*, 102627. [CrossRef]
47. Lu, C.P.; Hou, M.C.; Liu, Z.L.; Li, H.J.; Lu, C.Y. Variation Characteristic of NDVI and its Response to Climate Change in the Middle and Upper Reaches of Yellow River Basin, China. *IEEE J. Sel. Top. Appl. Earth Obs. Remote Sens.* **2021**, *14*, 8484–8496. [CrossRef]
48. Liu, J.; Wei, L.H.; Zheng, Z.P.; Du, J.L. Vegetation cover change and its response to climate extremes in the Yellow River Basin. *Sci. Total Environ.* **2023**, *905*, 167366. [CrossRef]
49. Liu, Y.; Tian, J.Y.; Liu, R.H.; Ding, L.Q. Influences of Climate Change and Human Activities on NDVI Changes in China. *Remote Sens.* **2021**, *13*, 4326. [CrossRef]
50. Lin, X.N.; Niu, J.Z.; Berndtsson, R.; Yu, X.X.; Zhang, L.; Chen, X.W. NDVI Dynamics and Its Response to Climate Change and Reforestation in Northern China. *Remote Sens.* **2020**, *12*, 4138. [CrossRef]
51. Hussain, A.; Hussain, I.; Ali, S.; Ullah, W.; Khan, F.; Rezaei, A.; Ullah, S.; Abbas, H.; Manzoom, A.; Cao, J.; et al. Assessment of precipitation extremes and their association with NDVI, monsoon and oceanic indices over Pakistan. *Atmos. Res.* **2023**, *292*, 106873. [CrossRef]
52. He, L.; Guo, J.B.; Yang, W.B.; Jiang, Q.O.; Chen, L.; Tang, K.X. Multifaceted responses of vegetation to average and extreme climate change over global drylands. *Sci. Total Environ.* **2023**, *858*, 159942. [CrossRef] [PubMed]
53. Nishant, N.; Sherwood, S.C. How Strongly Are Mean and Extreme Precipitation Coupled? *Geophys. Res. Lett.* **2021**, *48*, e2020GL092075. [CrossRef]
54. Bador, M.; Alexander, L.V. Future Seasonal Changes in Extreme Precipitation Scale with Changes in the Mean. *Earths Future* **2022**, *10*, e2022EF002979. [CrossRef]
55. Xu, J.X. Precipitation-vegetation coupling and its influence on erosion on the Loess Plateau, China. *Catena* **2005**, *64*, 103–116.
56. Holzman, M.E.; Carmona, F.; Rivas, R.; Niclòs, R. Early assessment of crop yield from remotely sensed water stress and solar radiation data. *ISPRS J. Photogramm. Remote Sens.* **2018**, *145*, 297–308. [CrossRef]
57. Kim, Y.; Kimball, J.S.; Zhang, K.; McDonald, K.C. Satellite detection of increasing Northern Hemisphere non-frozen seasons from 1979 to 2008: Implications for regional vegetation growth. *Remote Sens. Environ.* **2012**, *121*, 472–487. [CrossRef]
58. Zhang, Z.H.; Song, Y.Z.; Wu, P. Robust geographical detector. *Int. J. Appl. Earth Obs. Geoinf.* **2022**, *109*, 102782. [CrossRef]
59. Cremonese, E.; Filippa, G.; Galvagno, M.; Siniscalco, C.; Oddi, L.; di Cella, U.M.; Migliavacca, M. Heat wave hinders green wave: The impact of climate extreme on the phenology of a mountain grassland. *Agric. For. Meteorol.* **2017**, *247*, 320–330. [CrossRef]
60. Ying, H.; Zhang, H.Y.; Zhao, J.J.; Shan, Y.; Zhang, Z.X.; Guo, X.Y.; Wu, R.H.; Deng, G.R. Effects of spring and summer extreme climate events on the autumn phenology of different vegetation types of Inner Mongolia, China, from 1982 to 2015. *Ecol. Indic.* **2020**, *111*, 105974. [CrossRef]
61. Su, R.H.; Guo, E.L.; Wang, Y.F.; Yin, S.; Bao, Y.L.; Sun, Z.Y.; Mandula, N.; Bao, Y.H. Vegetation Dynamics and Its Response to Extreme Climate on the Inner Mongolian Plateau during 1982–2020. *Remote Sens.* **2023**, *15*, 3891. [CrossRef]
62. Richardson, A.D.; Hufkens, K.; Milliman, T.; Aubrecht, D.M.; Furze, M.E.; Seyednasrollah, B.; Krassovski, M.B.; Latimer, J.M.; Nettles, W.R.; Heiderman, R.R.; et al. Ecosystem warming extends vegetation activity but heightens vulnerability to cold temperatures. *Nature* **2018**, *560*, 368–371. [CrossRef]
63. Xiong, J.; Thenkabail, P.S.; Gumma, M.K.; Teluguntla, P.; Poehnelt, J.; Congalton, R.G.; Yadav, K.; Thau, D. Automated cropland mapping of continental Africa using Google Earth Engine cloud computing. *ISPRS J. Photogramm. Remote Sens.* **2017**, *126*, 225–244. [CrossRef]
64. Ghaderpour, E.; Vujadinovic, T. Change Detection within Remotely Sensed Satellite Image Time Series via Spectral Analysis. *Remote Sens.* **2020**, *12*, 4001. [CrossRef]
65. Jing, W.L.; Yang, Y.P.; Yue, X.F.; Zhao, X.D. A Spatial Downscaling Algorithm for Satellite-Based Precipitation over the Tibetan Plateau Based on NDVI, DEM, and Land Surface Temperature. *Remote Sens.* **2016**, *8*, 655. [CrossRef]
66. Gao, S.; Dong, G.; Jiang, X.; Nie, T.; Yin, H.; Guo, X. Quantification of Natural and Anthropogenic Driving Forces of Vegetation Changes in the Three-River Headwater Region during 1982–2015 Based on Geographical Detector Model. *Remote Sens.* **2021**, *13*, 4175. [CrossRef]
67. Gebremicael, T.G.; Mohamed, Y.A.; Van der Zaag, P. Attributing the hydrological impact of different land use types and their long-term dynamics through combining parsimonious hydrological modelling, alteration analysis and PLSR analysis. *Sci. Total Environ.* **2019**, *660*, 1155–1167. [CrossRef] [PubMed]
68. Amini, A. The role of climate parameters variation in the intensification of dust phenomenon. *Nat. Hazards* **2020**, *102*, 445–468. [CrossRef]
69. Zhong, S.; Qian, Y.; Zhao, C.; Leung, R.; Wang, H.L.; Yang, B.; Fan, J.W.; Yan, H.P.; Yang, X.Q.; Liu, D.Q. Urbanization-induced urban heat island and aerosol effects on climate extremes in the Yangtze River Delta region of China. *Atmos. Chem. Phys.* **2017**, *17*, 5439–5457. [CrossRef]
70. Lin, L.J.; Gao, T.; Luo, M.; Ge, E.J.; Yang, Y.J.; Liu, Z.; Zhao, Y.Q.; Ning, G.C. Contribution of urbanization to the changes in extreme climate events in urban agglomerations across China. *Sci. Total Environ.* **2020**, *744*, 140264. [CrossRef]

71. Georgescu, M.; Broadbent, A.M.; Wang, M.; Krayenhoff, E.S.; Moustaoui, M. Precipitation response to climate change and urban development over the continental United States. *Environ. Res. Lett.* **2021**, *16*, 044001. [CrossRef]
72. Deng, Z.F.; Wang, Z.L.; Wu, X.S.; Lai, C.G.; Liu, W.Q. Effect difference of climate change and urbanization on extreme precipitation over the Guangdong-Hong Kong-Macao Greater Bay Area. *Atmos. Res.* **2023**, *282*, 106514. [CrossRef]